SCIENTIFIC REPORTS

Synthesis of Pt/K$_2$CO$_3$/MgAlO$_x$–reduced graphene oxide hybrids as promising NO$_x$ storage–reduction catalysts with superior catalytic performance

Xueyi Mei[1], Qinghua Yan[1], Peng Lu[1], Junya Wang[2], Yuhan Cui[1], Yu Nie[1], Ahmad Umar[3,4] & Qiang Wang[1]

Pt/K$_2$CO$_3$/MgAlO$_x$–reduced graphene oxide (Pt/K/MgAlO$_x$–rGO) hybrids were synthesized, characterized and tested as a promising NO$_x$ storage and reduction (NSR) catalyst. Mg–Al layered double hydroxides (LDHs) were grown on rGO via *in situ* hydrothermal crystallization. The structure and morphology of samples were thoroughly characterized using various techniques. Isothermal NO$_x$ adsorption tests indicated that MgAlO$_x$–rGO hybrid exhibited better NO$_x$ trapping performance than MgAlO$_x$, from 0.44 to 0.61 mmol·g^{-1}, which can be attributed to the enhanced particle dispersion and stabilization. In addition, a series of MgAlO$_x$–rGO loaded with 2 wt% Pt and different loadings (5, 10, 15, and 20 wt%) of K$_2$CO$_3$ (denoted as Pt/K/MgAlO$_x$–rGO) were obtained by sequential impregnation. The influence of 5% H$_2$O on the NO$_x$ storage capacity of MgAlO$_x$–rGO loaded with 2 wt% Pt and 10% K$_2$CO$_3$ (2Pt/10 K/MgAlO$_x$–rGO) catalyst was also evaluated. In all, the 2Pt/10 K/MgAlO$_x$–rGO catalyst not only exhibited high thermal stability and NO$_x$ storage capacity of 1.12 mmol·g^{-1}, but also possessed excellent H$_2$O resistance and lean–rich cycling performance, with an overall 78.4% of NO$_x$ removal. This work provided a new scheme for the preparation of highly dispersed MgAlO$_x$–rGO hybrid based NSR catalysts.

Nitrous oxides (NO$_x$) are known as hazardous compounds and one of the main causes for the formation of highly toxic photochemistry smog and acid rain[1–3]. For the NO$_x$ emission control from automobile exhausts, three–way catalysts are highly efficient when the engines work at stoichiometric air/fuel ratio (A/F = 14.7). However, their efficiency diminishes severely in the presence of an excess of oxygen[4–8]. Thus, up to now, the NO$_x$ abatement for lean–burn engine emissions is still widely recognized as one of the most challenging problems[9–11].

The NO$_x$ storage and reduction (NSR) catalytic treatment appears to be a promising approach to remove NO$_x$ under the excess oxygen condition[12,13]. The NSR catalysts generally consist of three major components: precious metal (e.g. Pt, Pd, or Rh), alkali or alkaline earth metal oxide as NO$_x$ storage material (e.g. Ba, Sr, Ca, Li, K, or Na), and a high surface area support like γ–Al$_2$O$_3$[14–17]. During lean conditions, NO$_x$ was stored as nitrates (or nitrite), while during the short rich conditions, the stored NO$_x$ will be released and then selectively reduced to N$_2$[18–20]. Up to date, several groups of NSR catalysts have been developed[21]. However, each type of catalysts have their own shortcomings, such as the narrow range of operating temperatures, thermal degradation and deactivation by sulfur adsorption, etc refs 22, 23. For these reasons, extensive efforts are still being made to develop novel NSR catalysts.

Recently, well mixed transition–metal oxides derived from layered double hydroxides (LDHs) have been suggested to offer potential advantages over Pt/BaO/Al$_2$O$_3$ in NO$_x$ storage–reduction and assessed to be the new

[1]College of Environmental Science and Engineering, Beijing Forestry University, 35 Qinghua East Road, Haidian District, Beijing 100083, P. R. China. [2]Faculty of Environmental Science and Engineering, Kunming University of Science and Technology, Kunming, 650500, Yunnan, P. R. China. [3]Department of Chemistry, College of Science and Arts, Najran University, Najran–11001, Kingdom of Saudi Arabia. [4]Promising Centre for Sensors and Electronic Devices (PCSED), Najran University, Najran–11001, Kingdom of Saudi Arabia. Correspondence and requests for materials should be addressed to Q.W. (email: qiangwang@bjfu.edu.cn)
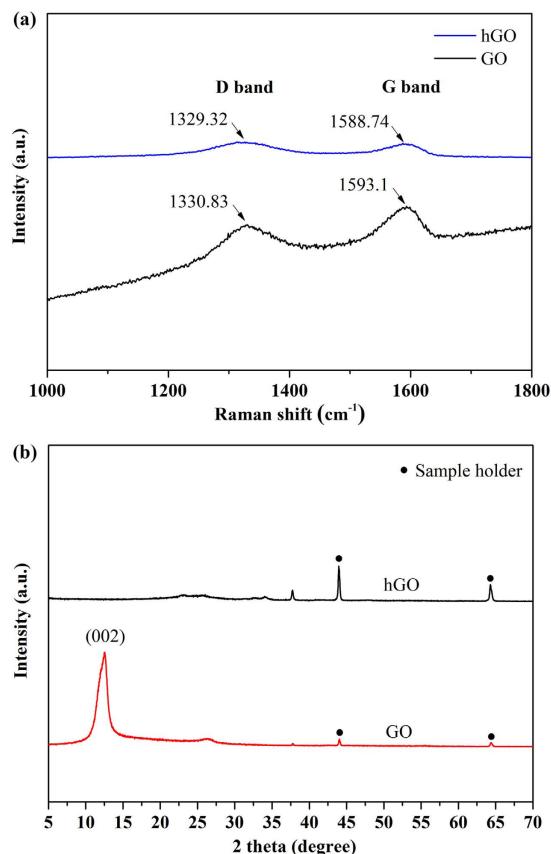
Figure 1. (**a**) Raman patterns of GO and hGO and (**b**) XRD patterns of GO and hGO.

generation of NSR catalysts[24,25]. LDH is a class of anionic clays[25]. The lamellar structure of LDH is based on positively charged brucite–like sheets with anions and water molecules intercalated between the layers[26,27]. For a long time, Mg–Al LDHs, which can be precursors to Mg–Al mixed oxides ($MgAlO_x$) have received significant attention for NO_x adsorption[24,28–30]. Takahashi et al.[28] reported that the NO_x storage material could be improved at high[28–30] temperature by using hydrotalcite–derived $MgAl_2O_4$ spinel as support. Especially, K–supported $MgAlO_x$ ($K/MgAlO_x$) showed improved NO_x adsorption. Park et al[24]. reported the Pt and K promoted hydrotalcite–based catalyst displayed better adsorption capacity, the NO_x storage capacity of which could be significantly increased to nearly $0.65 \, mmol \cdot g^{-1}$, by using 20% CH_3COOK as the precursors. Li et al.[31] also found that the addition of K enhances the NO_x storage capacity of hydrotalcite–derived MnMgAlO catalysts to a great extent compared with the corresponding K–free catalysts, from 0.27 to $0.92 \, mmol \cdot g^{-1}$, by using 20% KNO_3 as the precursor.

Recently, the growth of LDHs on various substrates has received considerable attention[32]. Particularly, graphene structures which possess huge surface area and can be made free–standing could provide a large number of actives sites for adsorption purpose[33]. Luckily, due to the negatively charged nature of graphene and positively charged nature of LDHs, the combination between these two 2D building blocks can be easily achieved by electrostatic interaction[34]. Various strategies have been used to fabricate LDH–GO hybrid materials, including directly mixing LDHs and GO[35], layer–by–layer self–assembly[36], and directly LDH formation on GO[32]. These LDH–GO hybrid materials have been used in supercapacitors[32,35,36], biosensors[37,38], water treatment[39], and CO_2 capture, etc refs 40, 41.

In this contribution, a novel NSR catalyst Pt/K/$MgAlO_x$–rGO with good NO_x storage capacity and excellent lean–rich cycling stability was developed by in situ grown of Mg–Al LDHs on rGO and the subsequent sequential impregnation of Pt and K_2CO_3. The influence of the addition of rGO on the NO_x storage capacity of $MgAlO_x$ based NSR catalysts was investigated. All samples were thoroughly characterized by XRD, XPS, SEM, TEM, FT–IR, Raman and BET analyses. The influences of Pt and K doping on the NO_x storage capacity of $MgAlO_x$–GO hybrids were also evaluated. Finally, the NO_x storage and reduction cycling performance and thermal stability of 2Pt/10K/$MgAlO_x$–GO hybrid catalyst were also tested.

Results and Discussion

Figure 1(a) shows the Raman spectra of GO and the GO treated by hydrothermal method at 120 °C under pH = 10 for 12 h (designated as hGO). It is well known that graphene exhibits two main characteristic peaks: the D band at ~1350 cm^{-1}, arising from a breathing mode of k–point photons of A_{1g} symmetry and the G band at ~1575 cm^{-1}, arising from the first order scattering of E_{2g} phonon of sp^2 C atoms[42]. In our present study, it can be seen that both GO and hGO exhibited a D band at 1330 cm^{-1} and a G band at 1593 cm^{-1}. It is also found that
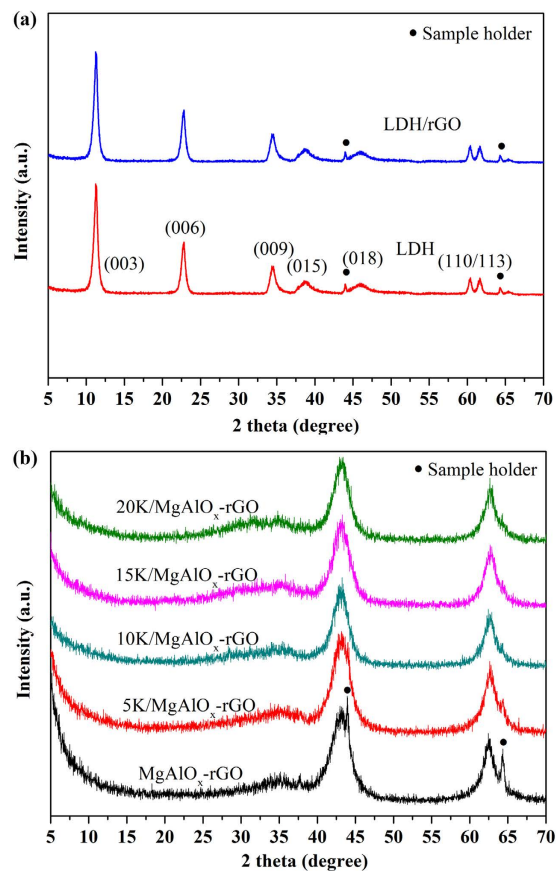
Figure 2. (**a**) XRD patterns of neat LDH, and LDH/rGO hybrid, and (**b**) XRD patterns of XK/MgAlOₓ–rGO hybrids (X = 5, 10, 15, and 20 wt%).

the hGO showed a relatively higher intensity of D to G band (1.01) than that of GO (0.93). These observations confirmed the formation of new graphitic domains after the hydrothermal treatment process[43]. The XRD patterns of dried GO and hGO were also shown in Fig. 1(b). As it is expected that the dried GO displayed a layered structure with an interlayer spacing of 0.86 nm corresponding to the feature diffraction peak at 10.2°, revealing the introduction of oxygen functional groups on the graphite sheets[44,45]. However, after treated with hydrothermal method under pH = 10, the hGO exhibited the major peak at about 23–24°. This gives an interlayer spacing of approximately 0.37–0.38 nm. This interlayer spacing is much smaller than that for GO (0.86 nm), and is closer to the (002) graphite peak of 0.336 nm[46]. Taken together, both Raman and XRD data suggested the evidence to support the formation of rGO under hydrothermal condition at pH = 10. Therefore, the obtained hybrid material was denoted as LDH/rGO.

The XRD patterns of neat LDH, and the as synthesized LDH/rGO are shown in Fig. 2(a). Neat LDH exhibited a hexagonal structure with sharp symmetric peaks for the (*003*), (*006*) and (*009*) planes and broad asymmetric peaks for (*015*) and (*018*) planes which are characteristic of hydrotalcites. The diffraction lines at about 60.5° and 61.5° are ascribed to the (*110*) and (*113*) reflections[47]. In the case of LDH/rGO, the diffraction peaks are similar to those of pristine LDH, but no shift in basal reflection peaks was observed. This suggests the similarity in the intercalation of CO_3^{2-} anions into the layer galleries between the pristine LDH and the distributed LDH grown on rGO[37]. Figure 2(b) shows the XRD patterns of K_2CO_3 doped MgAlOₓ–rGO (K/MgAlOₓ–rGO) samples with different loadings of K_2CO_3. These diffractograms showed two intense lines (43°, and 62.5°), which are typical to MgO–like phase or likely magnesia–alumina solid solution (JCPDS 45–946). No diffraction peaks corresponding to K–related species were observed. Many similar results have been reported that the K–containing species could hardly be recognized by XRD analysis[48–51]. So, it was deduced that the K_2CO_3 species were well dispersed on the support and probably existed in amorphous phase that may be below the XRD detection limit[48].

ATR–FTIR spectra of dried GO, neat LDH, and LDH/rGO hybrids are shown in Fig. 3(a). The absorption peaks at 3400 cm⁻¹ for the GO correspond to the stretching mode of O–H. The characteristic features for GO are the stretching vibrations of C=O (carboxylic acid) at 1677 cm⁻¹, C–O–C (epoxy) and C–O (alkoxy) at 925–1445 cm⁻¹, and C=C at 1575 cm⁻¹, originating from the skeletal vibrations of un–oxidized graphitic domains[52–56]. In all the spectra of neat LDH samples, a strong broad vibration band in the 3200 to 3600 cm⁻¹ range can be observed, which can be attributed to the O–H stretching vibration of water molecules and hydroxyl groups that belong to brucite layers. The band at 1624 cm⁻¹ was due to the H–O–H bending vibration. A strong band at 1360 cm⁻¹ was attributed to the carbonate group. The bands below 800 cm⁻¹ were ascribed to Al–O and Mg–O vibrations[57]. When combined, the peaks in the spectra of LDH/rGO are consistent with those of the LDH
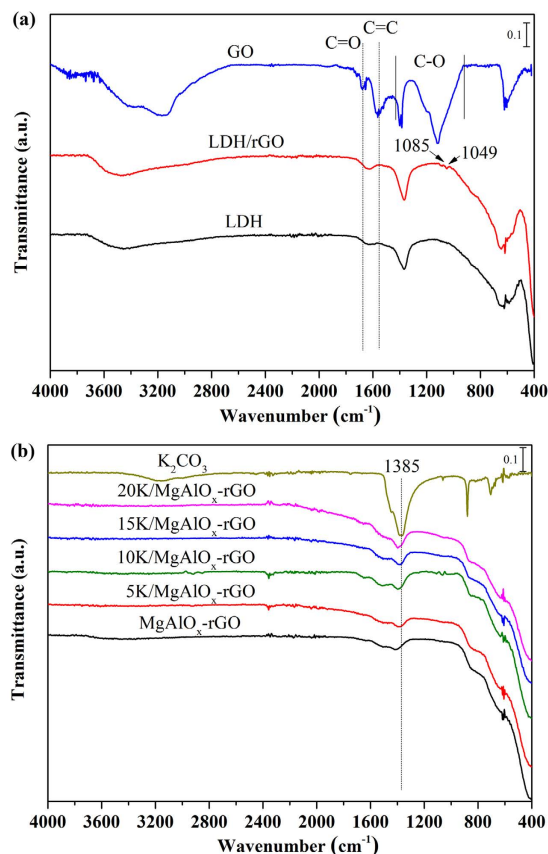
Figure 3. (**a**) ATR FT–IR spectra of GO, LDH, and LDH/rGO hybrids, and (**b**) ATR FT–IR spectra of XK/MgAlO$_x$–rGO (X = 5, 10, 15, and 20 wt%).

and GO, indicating the successful hybridization of rGO with LDH. As no information about K species was given by XRD results, thus ATR FT–IR technique was employed to investigate the states of K species, as shown in Fig. 3(b). The bulk K$_2$CO$_3$ used as the precursor of potassium salt shows the characteristic IR bands in the region of 1800–1000 cm^{-1}. When K was introduced, the K$_2$CO$_3$ species was clearly detected, with the characteristic peak located at 1385 cm^{-1} [58]. The intensity of this characteristic peak became stronger with the increase in K$_2$CO$_3$ loading.

The BET specific surface areas of MgAlO$_x$, MgAlO$_x$–rGO, 10 K/MgAlO$_x$, and 10 K/MgAlO$_x$–rGO were also investigated. The specific surface area of MgAlO$_x$–rGO hybrid was 230.6 m$^2 \cdot$g^{-1}, which was larger than that of neat MgAlO$_x$ (207.5 m$^2 \cdot$g^{-1}). It has been proven that the addition of rGO can decrease the aggregation of MgAlO$_x$, resulting in more exposed MgAlO$_x$ nanosheets and enlarged specific surface area[59]. After loading K$_2$CO$_3$, the specific surface area decreased a little for both 10 K/MgAlO$_x$ (199.1 m$^2 \cdot$g^{-1}) and 10 K/MgAlO$_x$–rGO (129.2 m$^2 \cdot$g^{-1}), probably due to the pore blocking by K$_2$CO$_3$.

The morphologies and structures of the GO and LDH were investigated by XRD and HR–TEM, as shown in Fig. 4. The SEM image of pure LDH (Fig. 4(a)) shows that the sample consist of a large number of LDH nanoplates, which have aggregated in a disordered fashion with a definite shape. The image in Fig. 4(b) shows that the pure LDH consists of abundant particles with a definite shape, which was of high quality in terms of crystallinity, and the mean size is determined to be ca. 100–200 nm. However, because of the high surface energy and strong van der Waals interactions, aggregated LDHs were observed. Figure 4(c) reveals that the GO nanosheets are curled and wrinkled just like a transparent corrugated voile due to the intrinsic nature of the GO nanosheets[60]. Closer observation of the HR–TEM image (Fig. 4(d)) shows the fringes at the edge of a flake, indicating the stacking of 2–3 monolayers. The inset SAED pattern of the GO shows the typical hexagonal crystal lattice which has a six–fold symmetry.

The LDH platelets are adsorbed on the surface of rGO nanosheets due to the electrostatic interaction between rGO and LDH[61]. Both LDH and rGO nanosheets were clearly observed was showed in Fig. 5, as indicated by the white arrows and black arrows, respectively. Form Fig. 5(b), it is clear that the LDH/rGO nanoplates are distributed on the surface of rGO nanosheets. Some LDH grew with *ab*–planes of the crystallites parallel to rGO, whereas some LDH grew with *ab*–planes perpendicular to rGO surface. Figure 5(c) reveals a marked contrast between the LDH nanoparticles and the underlying rGO. The thickness and the average particle size of the LDH nanoparticles were found to be ca. 10 and 50 nm, respectively. At higher magnification (Fig. 5(d)), it can be seen more clearly. The distribution of the LDH is not uniform because the rGO sheets capture the LDH mainly via reactive groups, and the active sites of rGO are not homogeneously distributed on the nanosheets[32].
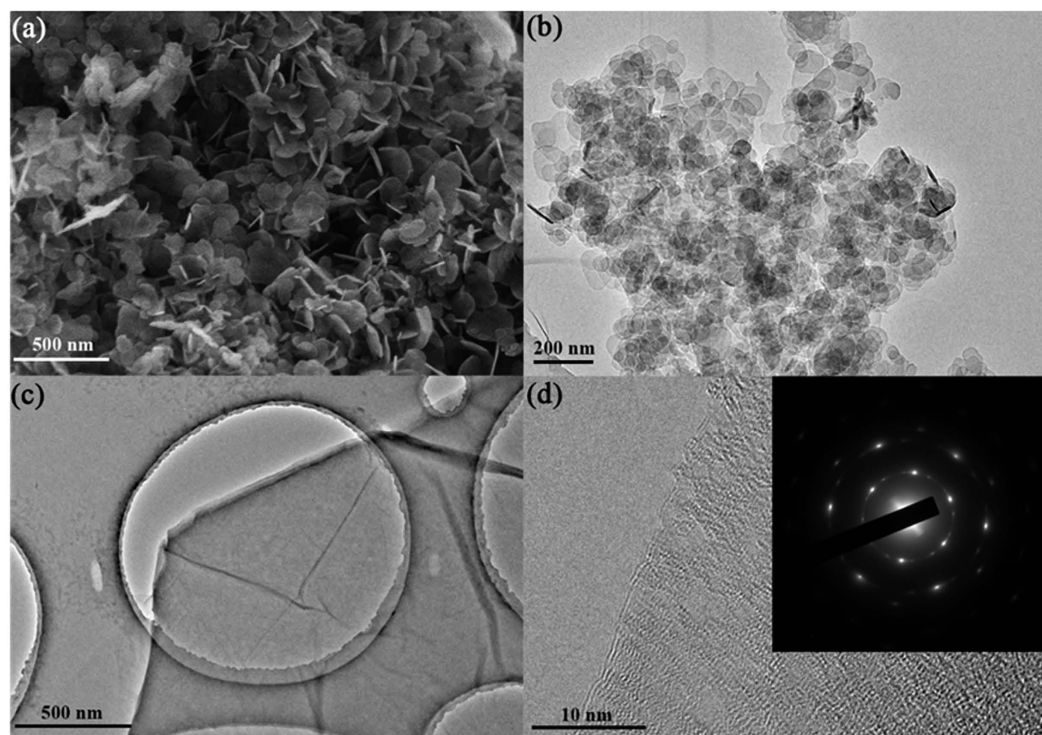
Figure 4. (**a**) FE–SEM of Mg–Al–CO$_3$ LDH, (**b**) HR–TEM image of Mg–Al–CO$_3$ LDH, (**c**) HR–TEM image of graphene oxide, and (**d**) HR–TEM image of graphene oxide with higher resolution, the inset shows SAED pattern of the GO.

As noble metals, such as Pt, plays a key role in the NO$_x$ storage and reduction cycles, it is of great interest to investigate its existence in detail. No relevant changes are introduced in the diffraction patterns with Pt incorporation (Fig. 6(a)), which might due to the high dispersion of Pt in the catalyst[62]. To further elucidate the existence of Pt, SEM–EDS was performed on the catalyst, and the images are displayed in Fig. 6(b). The SEM image is fully consistent with the XRD results. No Pt–containing crystals could be observed, suggesting Pt species that are so small and highly dispersed. However, the EDS analysis confirmed the existence of Pt with an average Pt loading of 2.87 ± 0.38 wt%. This value is somehow higher than that of the theoretical amount used for the preparation, which can be attributed to the detection limitation of EDS. Figure 6(c) and (d) show the HR–TEM images of the catalyst. In all cases the Pt nanoparticles are dispersed on the support surface (Fig. 6(c)), with an average of particle size of 2.7–3.5 nm being determined from the HR–TEM images (Fig. 5(d)). The d–spacing value of 0.227 nm coincides with that of fcc Pt (111)[63].

The NO$_x$ storage amount on MgAlO$_x$ was first measured by the isothermal storage of NO+O$_2$ at 250, 300, 350, and 400 °C, respectively, as shown in Fig. 7(a). The NO$_x$ concentration in the outlets first showed a sharp decrease during the first several min and then followed by a gradual increase as a function of time. The lowest values were reached after about 10–15 min for all temperature range (250–400 °C). The difference between inlet and outlet NO$_x$ concentration corresponded to the NO$_x$ stored on the catalyst. It took around 100 min for MgAlO$_x$ to become saturated. Particularly, the sample can quickly capture the NO$_x$ within the first ca. 10 min, reaching the lowest point (~250 ppm) at 350 °C. Upon calculation, a maximum value of adsorbed NO$_x$ species close to 0.44 mmol·g^{-1} catalyst was achieved at 350 °C. Since the reaction time was only 100 min and the reaction balance has not been reached yet. Both NO$_2$ storage and NO conversion to NO$_2$ occurred at the same time, therefore the NO conversion to NO$_2$ could not be calculated accurately. But for MgAlO$_x$, the NO to NO$_2$ conversion could be approximately estimated by the outlet NO$_2$/NO$_x$ value because the reaction was close to equilibrium. As shown in Fig. 7(b), it is clear that the conversion increased with the increase in testing temperature from 250 to 400 °C. However, pure MgAlO$_x$ without noble metal such as Pt showed low NO oxidation activity.

In our previous work, the addition of 7 wt% GO showed better NO$_x$ storage capacity due to decreasing the aggregation of LDO and resulting in more exposed LDO nanosheets[62]. Therefore, in this study rGO was also investigated as a supporting material to optimized the NO$_x$ storage capacity of neat LDH. Figure 7(c) exhibits the isothermal NO$_x$ storage performance of MgAlO$_x$ and MgAlO$_x$–rGO at 350 °C. For MgAlO$_x$–rGO hybrid, it exhibited quicker NO$_x$ uptake and higher NO$_x$ capture capacity than those of MgAlO$_x$. The NO$_x$ adsorption rate is very high and the reachable lowest NO$_x$ concentration was about 200 ppm. A maximum NO$_x$ storage value around 0.61 mmol·g^{-1} was obtained, even much higher than that of MgAlO$_x$ (0.44 mmol·g^{-1}). Therefore, these data suggest that the absolute NO$_x$ storage capacity of MgAlO$_x$ can be markedly improved by adding 7 wt% GO, which was used in the hydrothermal process for its functional surfaces, worked as a template for the nucleation of
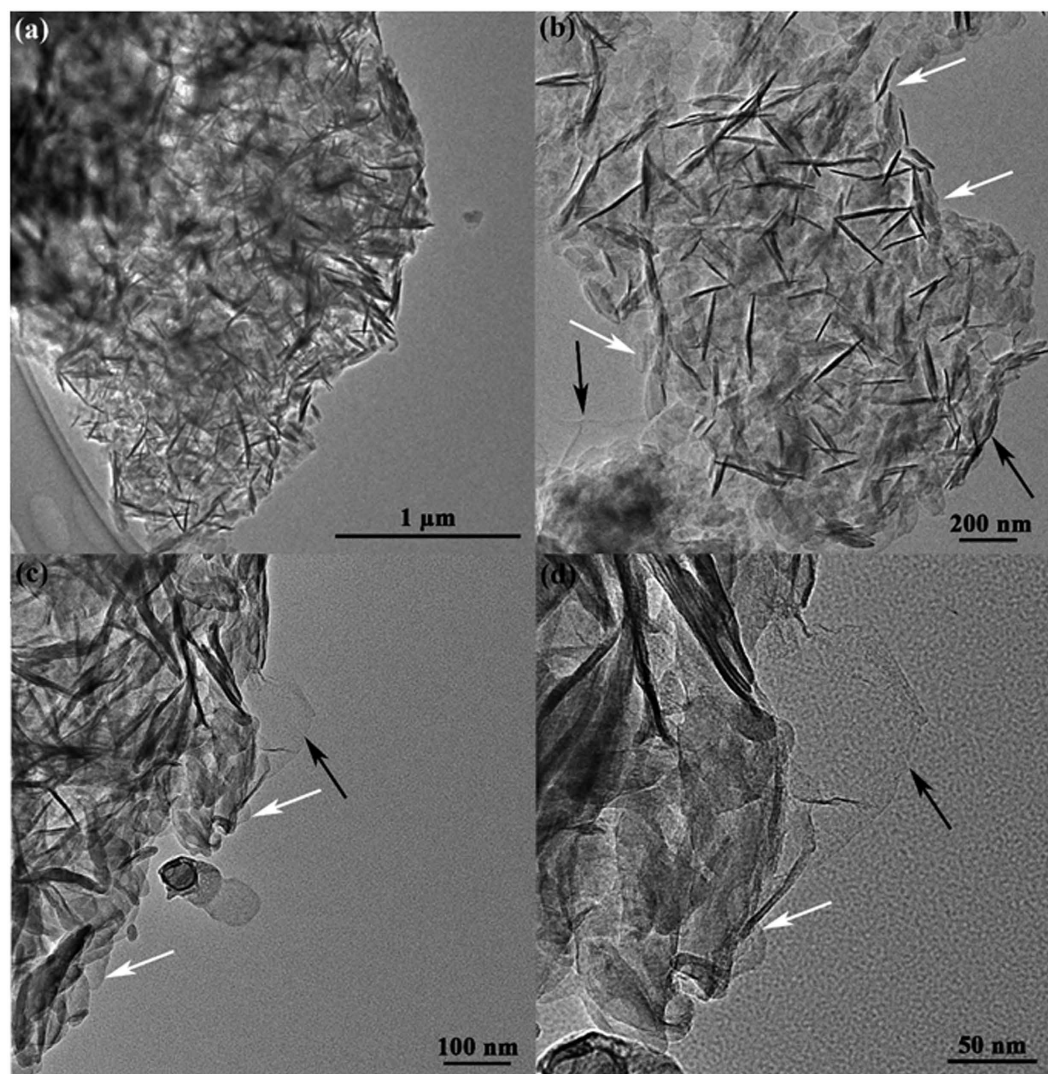
Figure 5. HR–TEM images of the LDH/rGO hybrids with different magnifications, (**a**) ×5000, (**b**) ×20000, (**c**) ×15000, and (**d**) ×15000.

Mg–Al LDHs and provided anchoring sites to the LDH nanosheets[64]. For LDH, the addition of K could remarkably improve their performance for NO_x storage[28,65].

The presence of K increased the mobility of surface oxygen species on the catalysts[66] and enhanced the formation of low melting–point compounds[67]. Therefore, the influence of K doping has been investigated over $MgAlO_x$–rGO at 350 °C, as shown in Fig. 7(d). In this contribution, K_2CO_3 was regarded as the precursor material. For the samples with increasing the loading of K_2CO_3, the overall amount of NO_x stored was enhanced significantly and the reachable lowest NO_x concentration was about 100 ppm when the K loading was increased to 10 wt%. Meanwhile, the NO_x storage became a rather slow process and the highest NO_x storage amount was improved to 0.81 mmol·g^{-1}. However, the additional K did not provide further enhancement in the amount of stored NO_x. At K loading of 15 and 20 wt%, the overall NO_x storage activity decreased slightly. The presence of more bulk or bulk–like K_2CO_3 in these samples makes NO_x storage more difficult due to the gradually increased surface to bulk diffusion resistance. Finally, the NO_x storage amount of neat $MgAlO_x$ can be significantly promoted from 0.44 to 0.81 mmol·g^{-1} with the addition of 7 wt% GO and 10 wt% K_2CO_3.

Precious metals represent an obvious choice for both the NO oxidation to NO_2 during lean condition and the adsorbed NO_x reduction during rich condition for the NSR catalysts, due to their unparalleled red–ox activity, and Pt has been the primary oxidation catalyst choice for NSR samples to date. Thus, the influence of Pt doping on 10 K/$MgAlO_x$ and 10 K/$MgAlO_x$–rGO hybrids was also studied, as shown in Fig. 8(a). In comparison to Pt unloaded samples, all Pt loaded samples show much higher NO_x storage activity at 350 °C, which was increased from 0.44 and 0.61 mmol·g^{-1} to 0.85 and 1.12 mmol·g^{-1}, respectively. This improvement in NO_x storage capacity can be ascribed to the promoted NO oxidation to NO_2 by Pt, and highly dispersed Pt in the catalyst. Moreover, the containing Mg would help Pt to be well dispersed on the supports, leading to the increase in NO_x storage performance[8]. Figure S1 further confirmed the excellent NO_x storage capacity and NO oxidation in obtained
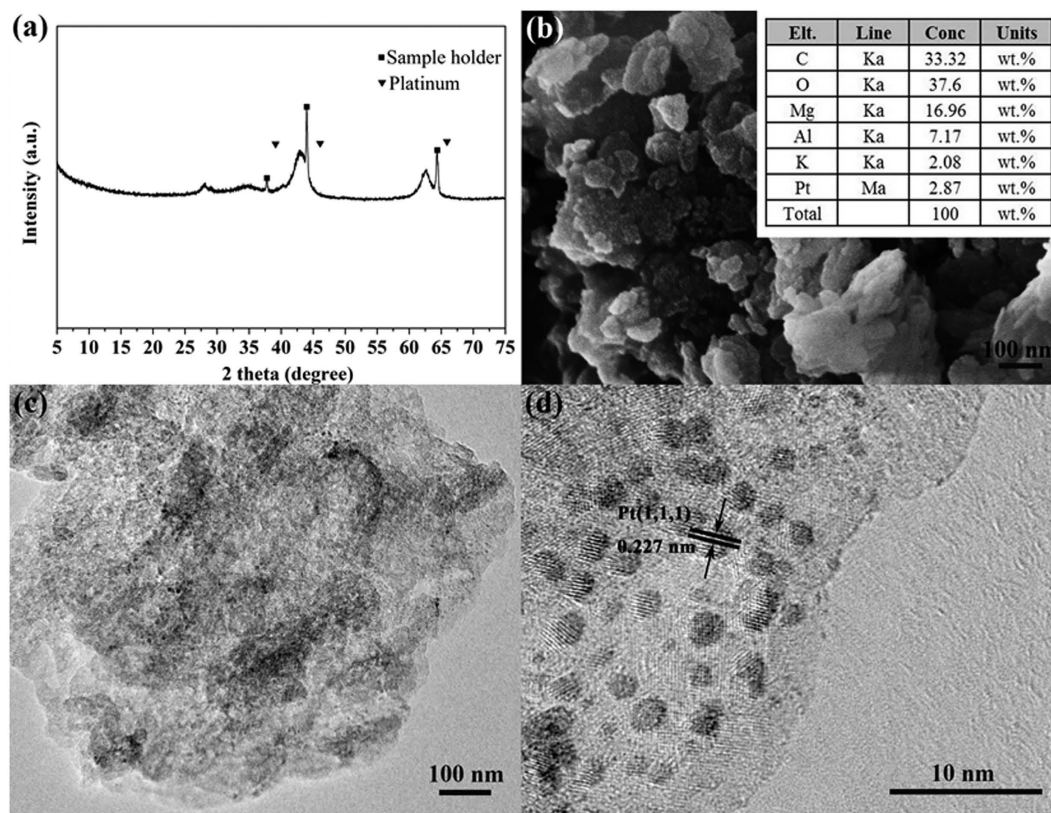
Figure 6. (**a**) XRD patterns of 2Pt/10 K/MgAlO$_x$–rGO catalyst, (**b**) SEM–EDS analyses of 2Pt/10 K/MgAlO$_x$–rGO catalyst, (**c**) TEM image of 2Pt/10 K/MgAlO$_x$–rGO catalyst, (**d**) TEM image of 2Pt/10 K/MgAlO$_x$–rGO catalyst with higher resolution.

2Pt/10 K/MgAlO$_x$–rGO catalyst during the whole reaction through plotting the NO, NO$_2$, NO$_x$, and the ratio of NO/NO$_2$ in the outlet.

H$_2$O is one of the main components in the vehicle exhausts and often affects the storage and regeneration performance of NSR catalysts. Previous investigations have shown that the presence of H$_2$O affect the NO$_x$ storage capacity[68,69]. Therefore, the H$_2$O poisoning effect on Pt/K/MgAlO$_x$–rGO catalyst was then studied. The influence of 5% H$_2$O on NO$_x$ storage over Pt/K/MgAlO$_x$–rGO catalyst at 350 °C is shown in Fig. 8(b). There is an almost complete capture of NO$_x$ for both conditions at the beginning. However, the saturation concentration is lower and the stability is higher in the absence of H$_2$O. From the inset of Fig. 8(b), it is evident that only slightly less NO$_x$ is stored when introduced 5% H$_2$O, from 1.12 to 1.02 mmol·g^{-1}, which is consistent with previous studies[68,69]. The common agreement in the literature is that the water vapor reduces the NO$_x$ storage capacity and leads to catalyst deactivation by decreasing the number of available active sites. The results demonstrated that although Pt/K/MgAlO$_x$–rGO was also slightly effected by 5% H$_2$O, its performance is still much better than that of Pt/K/MgAlO$_x$.

Figure 9(a) depicts the NO$_x$ concentration (ppm) profiles of the inlet and outlet gases over 2Pt/10 K/MgAlO$_x$–rGO catalyst during the NO$_x$ storage and reduction cyclic reaction at 350 °C. At beginning of the lean phase (6 min), a sharp NO$_x$ removal peak appeared immediately after the 2Pt/10 K/MgAlO$_x$–rGO contact was in contact with the gas mixture of NO+O$_2$, which indicated a nearly complete adsorption and/or conversion of NO$_x$ on the catalyst. The NO$_x$ profiles obtained during the lean cycle showed almost the same shape, and the NO$_x$ level reached a more or less constant value afterwards. Meanwhile, the NO$_x$ concentration decreased slowly with time and reached 150 ppm at the end of the lean phase. This is far below the inlet NO$_x$ concentration of 700 ppm, showing a large amount of NO$_x$ was stored. When it was switched to the rich phase (1 min), a quick increase in NO$_x$ concentration was observed in the first few seconds. This may be attributed to two reasons. One is that the rate of adsorption of NO$_x$ decreased when oxygen was cut off. The other is that in the first few seconds of rich phase, a certain amount of oxygen remained on the Pt[70]. Because of the high reductive activity of Pt, the main product was N$_2$ (~230 ppm) during rich cycles (Fig. 9(b)). Due to the limit of experimental condition, the N$_2$O could not be calibrated accurately. But the intensity of N$_2$O was very low compared with N$_2$ in the present results (as shown in Fig. S2) and the similar discussion has been reported by other literature[6,7]. Overall, more than 78.40% of NO$_x$ was removed during the whole lean–rich cycling tests.

The nature of the active species present on the surface is important for establishing the properties of the catalyst. For this purpose, the XPS analysis has been performed in order to obtain information about the surface composition of the obtained catalysts. Figure 10 shows the typical XPS spectra of 2Pt/10 K/MgAlO$_x$–rGO. In Fig. 10(a), the spectrum was deconvoluted into three components labelled as 1, 2 and 3 with respective binding energies of 71.55, 74.0, and 78.16 eV. The relative intensities (%) of the three components were 9.9, 84.7 and 5.4%,
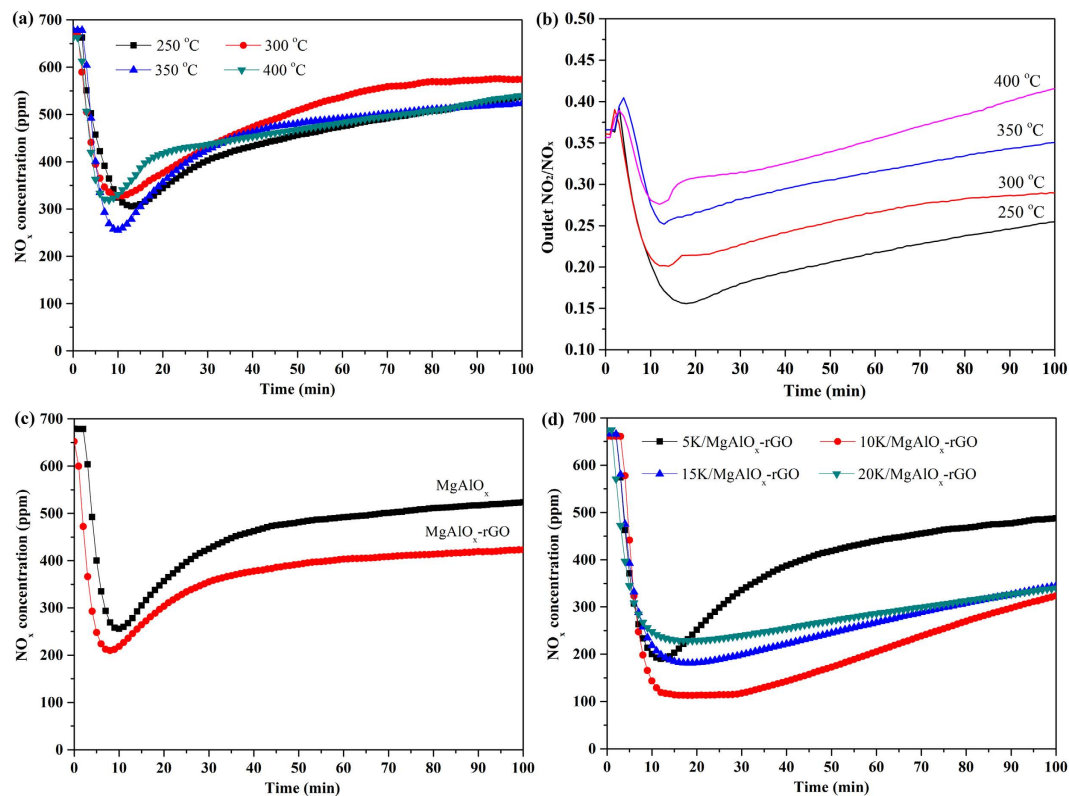
Figure 7. (**a**) Isothermal NO_x storage over $MgAlO_x$ at 250, 300, 350, and 400 °C, (**b**) Outlet NO_2/NO_x over $MgAlO_x$ at 250, 300, 350, and 400 °C, (**c**) isothermal NO_x storage over $MgAlO_x$ and $MgAlO_x$–rGO at 350 °C, (**d**) isothermal NO_x storage over $XK/MgAlO_x$–rGO (X = 5, 10, 15, and 20 wt%) at 350 °C.
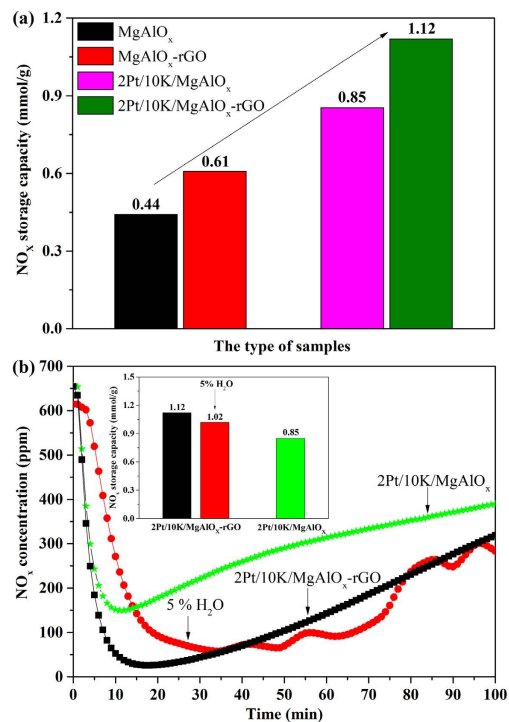

Figure 8. (**a**) Isothermal NO_x storage over $2Pt/10K/MgAlO_x$, $2Pt/10K/MgAlO_x$–rGO catalysts and the influence of 5% H_2O on $2Pt/10K/MgAlO_x$–rGO catalysts tested at 350 °C. (**b**)The NO_x storage capacities of $MgAlO_x$, $MgAlO_x$–rGO, $2Pt/10K/MgAlO_x$, and $2Pt/10K/MgAlO_x$–rGO catalysts tested at 350 °C.

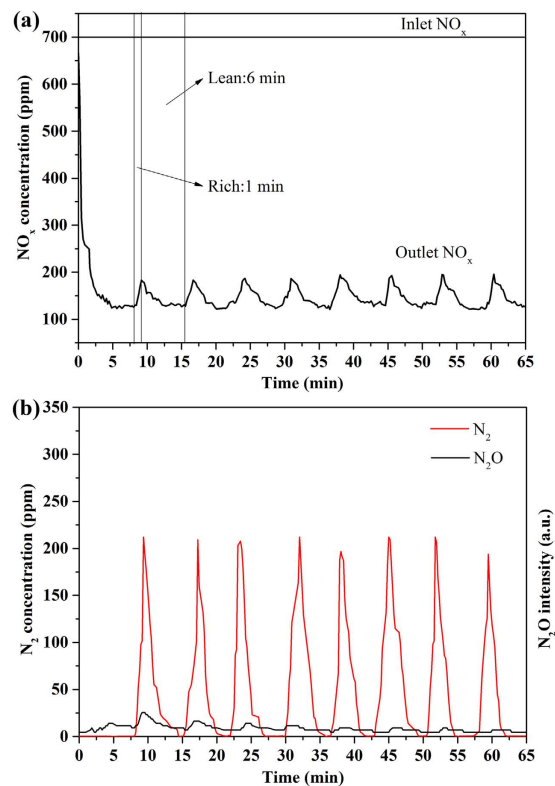**Figure 9.** (**a**) Evolution of effluent NO_x during lean–rich cycling tests over $2Pt/10\,K/MgAlO_x$–rGO catalyst at $350\,°C$, and (**b**) evolution of effluent N_2 and N_2O during lean–rich cycling tests over $2Pt/10\,K/MgAlO_x$–rGO catalyst at $350\,°C$.

respectively. The Pt-$4f_{7/2}$ signal at $71.55\,eV$ can be assigned to zero-valent platinum. The relative shift from the value of $70.8\,eV$ for the bulk metal is probably due to a contribution from metal-support interaction or small cluster-size effects[71]. The signal at 74.0 and $78.1\,eV$ could be ascribed to Pt^{2+} and Pt^{4+} oxidation states[72]. Oxygen chemisorption easily occurs at step and kink sites present on the surface of Pt clusters[73]. For the calcined catalyst, the Al $2p$ signals labelled as 1 and 2 were adjusted by using two components, as shown in Fig. 10(b). The first one, occurring around at $74.23\,eV$, is assigned to octahedrally coordinated Al^{3+}, whereas the second one, occurring around $73.41\,eV$ must be assigned to tetrahedrally coordinated Al^{3+}[74]. The intensity of the octahedrally coordinated Al^{3+} (81.68%) is higher than that of tetrahedrally coordinated Al^{3+} (16.10%). That may be assigned to the "memory effect" of LDH after exposure in the air for a long time[75]. Figure 10(c) displayed the binding energy of Mg $1s$ in the obtained catalyst. The peak located around $1304.28\,eV$ must be assigned to Mg^{2+} in periclase MgO structure[76].

The thermal stability of catalyst is another important issue. To investigate this, GO, $MgAlO_x$, $MgAlO_x$–GO and $2Pt/10\,K/MgAlO_x$–GO were tested in the TGA in the temperature range of 50–$700\,°C$ and in the presence of air, as shown in Fig. 11. The data indicates that GO is only thermally stable up to $400\,°C$. When the temperature was higher than $400\,°C$, GO started to decompose quickly, with a total weight loss of ca. 84.8% at $650\,°C$. This data suggested that neat GO is not thermally stable. The weight decrease of $MgAlO_x$ was only 16.92% in the temperature range of 50–$700\,°C$, which was due to the loss of loosely held water in the interlayer pace[77]. While once GO was hybridized with $MgAlO_x$, its thermal stability was significantly improved. Moreover, the $2Pt/10\,K/MgAlO_x$–rGO catalyst also showed excellent thermal stability, the decrease of which was approximately 14% in the temperature range of 50–$700\,°C$. There was only a slight decrease in weight with increasing the calcination temperature from 50 to $700\,°C$. So the thermal stability of the catalyst is not considered as a problem when the operating temperature of this novel catalyst is only ca. $350\,°C$. Taking its thermal and cycling stability into consideration, $2Pt/10\,K/MgAlO_x$–rGO displayed great potential to work as a NSR catalyst with improved NO_x storage ability.

Conclusion

In this contribution, a novel NSR catalyst $Pt/K/MgAlO_x$–rGO with good NO_x storage capacity and excellent lean–rich cycling stability was developed by *in situ* grown of Mg–Al LDHs on rGO and the subsequent sequential impregnation of Pt and K_2CO_3. Mg–Al LDHs were grown on rGO via *in situ* hydrothermal crystallization. The Pt nanoparticles were well dispersed with an average particle size of ca. 2.7–$3.5\,nm$. Isothermal NO_x storage tests demonstrated that the optimal operating temperature for $MgAlO_x$ was $350\,°C$. By introducing only $7\,wt\%$ of GO, the NO_x storage capacity of neat $MgAlO_x$ was significantly improved from 0.44 to $0.61\,mmol\cdot g^{-1}$, which can be attributed to the enhanced particle dispersion and stabilization. By impregnating $2\,wt\%$ Pt and $10\,wt\%$ K_2CO_3, the NO_x storage capacity was further increased to $1.12\,mmol\cdot g^{-1}$. We also demonstrated that our newly developed
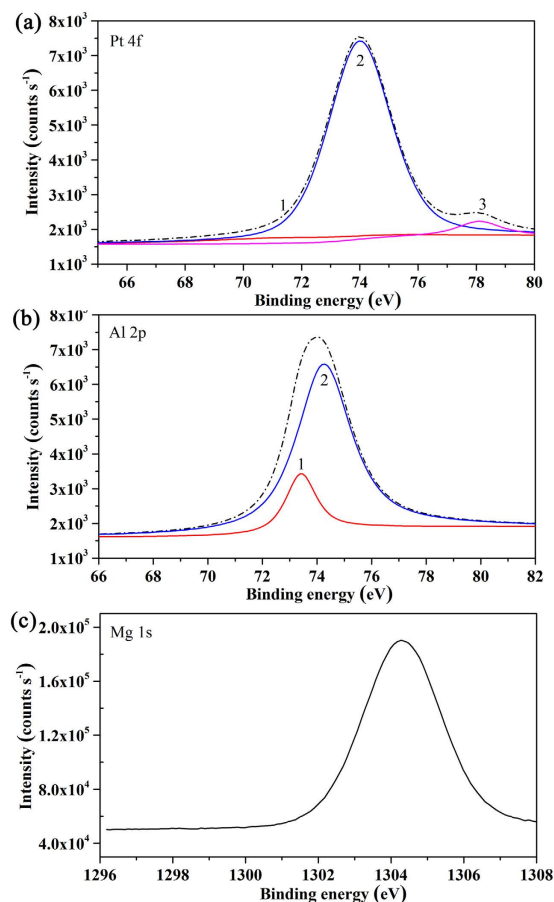
Figure 10. XPS analyses of synthesized 2Pt/10 K/MgAlO$_x$–rGO catalysts.
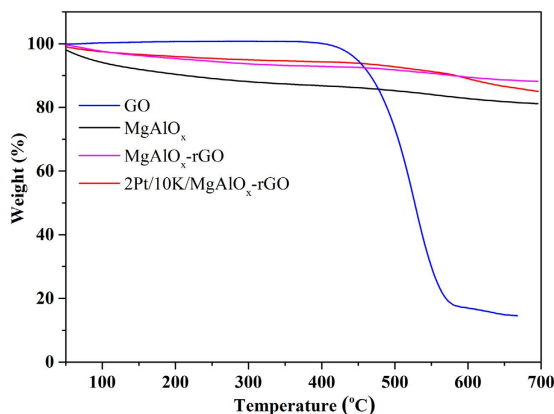

Figure 11. TGA analyses of synthesized GO, MgAlO$_x$, MgAlO$_x$–rGO, and 2Pt/10 K/MgAlO$_x$–rGO catalysts.

2Pt/10 K/MgAlO$_x$–rGO catalyst possesses excellent H$_2$O resistance and thermal stability. The obtained Pt/K/MgAlO$_x$–rGO catalyst also exhibited excellent lean–rich cycling performance, with an overall 78.4% of NO$_x$ removal.

Methods

Preparation of Mg–Al–CO$_3$ LDH.   LDH with Mg/Al = 3 was prepared using a hydrothermal procedure. In the method, 100 mL aqueous salt solution containing a mixture of 0.075 mol Mg(NO$_3$)$_2$·6H$_2$O and 0.025 mol Al(NO$_3$)$_3$·9H$_2$O was added drop–wise into a 100 mL aqueous solution containing 0.05 mol Na$_2$CO$_3$. In the meantime, the pH of the precipitation was controlled at 10 using a 4 M NaOH solution. The resulting mixture was hydrothermal treated at 120 °C for 12 h. It was then filtered and washed with deionized water until pH of the wash water became 7, and washed with acetone for several times, followed by drying at 60 °C.

Preparation of Mg–Al LDH/rGO hybrid. Firstly, the GO used in this study were prepared by modified Hummers method as described in our previous work[62]. The Mg–A1–CO$_3$ LDH/rGO hybrids were prepared via a hydrothermal method. In the method, 50 mL aqueous salt solution containing a mixture of 0.0375 mol Mg(NO$_3$)$_2$·6H$_2$O and 0.0125 mol Al(NO$_3$)$_3$·9H$_2$O was added drop–wise to another 250 mL solution containing 0.025 mol Na$_2$CO$_3$ and 200 mL GO dispersion (1 g·L^{-1}) under vigorous stirring at room temperature. The pH of the mixture was kept constant at 10 by adding a 4 M NaOH solution. The resulting mixture was hydrothermal treated at 120 °C for 12 h. It was then filtered and washed with deionized water until pH of the wash water became 7, and washed with acetone for several times, followed by dring at 60 °C in an oven. The obtained samples were designated as LDH/rGO.

Preparation of Pt/K/MgAlO$_x$–rGO. The Pt/K/MgAlO$_x$–rGO catalysts were prepared using a successive impregnation method. LDH/rGO was first pretreated at 400 °C in air for 5 h to obtain MgAlO$_x$–rGO hybrids. Next, the obtained MgAlO$_x$–rGO support was first impregnated with H$_2$PtCl$_6$·6H$_2$O ethanol solution (100 g·L^{-1}), dried at 60 °C for overnight, and calcined in air at 400 °C for 5 h. The sample was then impregnated with K$_2$CO$_3$ ethanediol solution (10 g·L^{-1}), followed by drying at 60 °C and calcining at 400 °C for 5 h. The loading of Pt was 2 wt%, and the loading of K$_2$CO$_3$ was controlled to be 5, 10, 15, and 20 wt%, respectively. The obtained catalysts were denoted as 2Pt/XK/MgAlO$_x$–rGO, where 2 and X represent the weight loading of Pt and K$_2$CO$_3$, respectively. XK/MgAlO$_x$–rGO samples were also prepared similarly for comparison.

Characterization. The phase structure and morphology of the samples were characterized by powder X–ray diffractometer (XRD, Shimadzu XRD–7000) with Cu Kα radiation and a power of 40 kV × 30 mA, X–ray photoelectron spectra (XPS) were recorded on a Thermo escalab 250Xi spectrometer equipped with A1 Kα X–ray source, a scanning electron microscope (FE–SEM, SU–8010), and a high resolution transmission electron microscopy (HR–TEM, JEOL 2010). Raman spectra were obtained on a Renishaw inVia Raman spectrometer with 532 nm wavelength incident laser light. Attenuated total reflectance–Fourier transform infrared spectroscopy (ATR–FTIR, Bruker VERTEX 70) was used to identify the functional groups of samples. BET specific surface areas were measured with a physisorption analyzer (SSA–7000, Builder). The weight loss of samples were measured using a Q50 TGA analyser (TA Instruments, N$_2$ flow rate = 60 mL·min^{-1}) in the temperature range of 50–700 °C.

NO$_x$ storage and reduction reaction. For NO$_x$ storage reaction, experiments were carried out in a fixed bed reactor (10 mm internal diameter) under atmospheric pressure. All gases except H$_2$O were introduced into the reactor via several mass flow controllers (Brooks Instruments). Liquid water was continuously added using a syringe pump (Lead fluid, TYD01) into a stainless steel tube wrapped with a temperature–controlled heating tape, in which the water vapor was generated. An on–line NO–NO$_2$–NO$_x$ analyser (Thermo Scientific 42i–HL, USA) was used to measure the concentration of NO, NO$_2$ and NO$_x$ in the outlet gas. The NO$_x$ storage capacity (NSC) was calculated by integrating the concentration curves of NO$_x$ when steady state was reached according to the following equation (1).

$$NSC = \frac{\int_0^{t_s} (NO_{x,in} - NO_{x,out})\,dt}{m_{cat}}$$

(1)

For each test, the time span is about 100 min and 0.2 g sample that was pre–calcined at 400 °C for 5 h in air was employed. Alternative lean/rich cyclic NO$_x$ storage and reduction was performed in the same reactor described as above under cyclic operation. Totally 8 cycles of 6 min lean and 1 min rich were applied, and 0.2 g of sample was used to measure the activity. NO$_x$ concentrations in both inlet and outlet were measured with an on–line quadrupole mass spectrometer (QGA, Hidden, UK). The mixture gas consisted of a continuous flow of 700 ppm NO$_x$ (430 ppm NO and 270 ppm NO$_2$), 10% O$_2$ (for lean condition only), 3.5% H$_2$ (for rich condition only), 5% H$_2$O (for evaluating the poisoning effect of H$_2$O only) and Ar as the balance gas, with a flow rate of 100 mL·min^{-1} (GHSV = 15000 h^{-1}). The reaction temperature was controlled at 250, 300, 350, and 400 °C, respectively.

References
1. Yoon, D. Y. *et al.* NO oxidation activity of Ag-doped perovskite catalysts. *J. Catal.* **319,** 182 (2014).
2. Heo, I. *et al.* Activity and thermal stability of Rh-based catalytic system for an advanced modern TWC. *Appl. Catal. B: Environ.* **121,** 75 (2012).
3. Heo, I. *et al.* Combination of photocatalysis and HC/SCR for improved activity and durability of DeNO$_x$ catalysts. *Environ. Sci. Technol.* **47,** 3657 (2013).
4. Park, J.-H., Park, S. J. & Nam, I.-S. Fast colorimetric assay for screening NSR catalyst. *Catal. Surv. Asia* **14,** 11 (2010).
5. Farrauto, R. J. & Heck, R. M. Catalytic converters: state of the art and perspectives. *Catal. Today* **51,** 351 (1999).
6. Wang, Q., Sohn, J. H. & Chung, J. S. Thermally stable Pt/K$_2$Ti$_2$O$_5$ as high-temperature NO$_x$ storage and reduction catalyst. *Appl. Catal. B: Environ.* **89,** 97 (2009).
7. Wang, Q. & Chung, J. S. NO$_x$ storage and reduction over Cu/K$_2$Ti$_2$O$_5$ in a wide temperature range: Activity, characterization, and mechanism. *Appl. Catal. A: Gen.* **358,** 59 (2009).
8. Jeong, S., Youn, S. & Kim, D. H. Effect of Mg/Al ratios on the NO$_x$ storage activity over Pt-BaO/Mg–Al mixed oxides. *Catal. Today* **231,** 155 (2014).
9. Ogura, M. *et al.* Stabilization of bare divalent Fe(II) cations in Al-rich beta zeolites for superior NO adsorption. *J. Catal.* **315,** 1 (2014).
10. Peng, Y., Si, W., Li, J., Crittenden, J. & Hao, J. Experimental and DFT studies on Sr-doped LaMnO$_3$ catalysts for NO$_x$ storage and reduction. *Catal. Sci. Technol.* **5,** 2478 (2015).
11. Gogurla, N., Sinha, A. K., Santra, S., Manna, S. & Ray, S. M. Multifunctional Au-ZnO plasmonic nanostructures for enhanced UV photodetector and room temperature NO sensing devices. *Sci. Rep.* **4,** 6483 (2014).
12. Matsumoto, S. DeNO$_x$ catalyst for automotive lean-burn engine. *Catal. Today* **29,** 43 (1996).

13. Shinjoh, H., Takahashi, N., Yokota, K. & Sugiura, M. Effect of periodic operation over Pt catalysts in simulated oxidizing exhaust gas. *Appl. Catal. B: Environ.* **15,** 189 (1998).
14. Liu, Y., Meng, M., Li, X.-G., Guo, L.-H. & Zha, Y.-Q. NO_x storage behavior and sulfur-resisting performance of the third-generation NSR catalysts $Pt/K/TiO_2–ZrO_2$. *Chem. Eng. Res. Des.* **86,** 932 (2008).
15. Xiao, J., Li, X., Deng, S., Wang, F. & Wang, L. NOx storage-reduction over combined catalyst $Mn/Ba/Al_2O_3–Pt/Ba/Al_2O_3$. *Catal. Commun.* **9,** 563 (2008).
16. Casapu, M. *et al.* Comparative study of structural properties and NO_x storage-reduction behavior of $Pt/Ba/CeO_2$ and $Pt/Ba/Al_2O_3$. *Appl. Catal. B: Environ.* **78,** 288 (2008).
17. Piacentini, M., Maciejewski, M. & Baiker, A. NOx storage-reduction behavior of $Pt-Ba/MO_2$ ($MO_2 = SiO_2$, CeO_2, ZrO_2) catalysts. *Appl. Catal. B: Environ.* **72,** 105 (2007).
18. Elbouazzaoui, S., Corbos, E. C., Courtois, X., Marecot, P. & Duprez, D. A study of the deactivation by sulfur and regeneration of a model NSR $Pt/Ba/Al_2O_3$ catalyst. *Appl. Catal. B: Environ.* **61,** 236 (2005).
19. Sedlmair, C., Seshan, K., Jentys, A. & Lercher, J. A. Studies on the deactivation of NO_x storage-reduction catalysts by sulfur dioxide. *Catal. Today* **75,** 413 (2002).
20. Engström, P., Amberntsson, A., Skoglundh, M., Fridell, E. & Smedler, G. Sulphur dioxide interaction with NO_x storage catalysts. *Appl. Catal. B: Environ.* **22,** L241 (1999).
21. Roy, S. & Baiker, A. NO_x Storage-Reduction Catalysis: From Mechanism and Materials Properties to Storage-Reduction Performance. *Chem. Rev.* **109,** 4054 (2009).
22. Castoldi, L., Nova, I., Lietti, L. & Forzatti, P. Study of the effect of Ba loading for catalytic activity of $Pt–Ba/Al_2O_3$ model catalysts. *Catal. Today* **96,** 43 (2004).
23. Piacentini, M., Maciejewski, M. & Baiker, A. Pt-Ba/alumina NO_x storage-reduction catalysts: Effect of Ba-loading on build-up, stability and reactivity of Ba-containing phases. *Appl. Catal. B: Environ.* **59,** 187 (2005).
24. Park, S. J. *et al.* Hydrotalcite as a support for NO_x trap catalyst. *Top. Catal.* **53,** 57 (2010).
25. Yang, R., Gao, Y., Wang, J. & Wang, Q. Layered double hydroxide (LDH) derived catalysts for simultaneous catalytic removal of soot and NO_x. *Dalton T.* **43,** 10317 (2014).
26. Wang, Q. & O'Hare, D. Recent advances in the synthesis and application of layered double hydroxide (LDH) nanosheets. *Chem. Rev.* **112,** 4124 (2012).
27. Wang, Z. *et al.* Co-Mn-Al Nonstoichiometric Spinel-Type Catalysts Derived from Hydrotalcites for the Simultaneous Removal of Soot and Nitrogen Oxides. *Sci. Adv. Mater.* **5,** 1449 (2013).
28. Takahashi, N., Matsunaga, S. I., Tanaka, T., Sobukawa, H. & Shinjoh, H. New approach to enhance the NO_x storage performance at high temperature using basic $MgAl_2O_4$ spinel support. *Appl. Catal. B: Environ.* **77,** 73 (2007).
29. Silletti, B. A. *et al.* A novel $Pd/MgAlO_x$ catalyst for NO_x storage-reduction. *Catal. Today* **114,** 64 (2006).
30. Fornasari, G. *et al.* Novel low temperature NO_x storage-reduction catalysts for diesel light-duty engine emissions based on hydrotalcite compounds. *Catal. Today* **75,** 421 (2002).
31. Li, Q. *et al.* Multifunctional hydrotalcite-derived $K/MnMgAlO$ catalysts used for soot combustion, NO_x storage and simultaneous soot–NO_x removal. *Chem. Eng. J.* **184,** 106 (2012).
32. Huang, S. *et al.* Immobilization of Co–Al layered double hydroxides on graphene oxide nanosheets: growth mechanism and supercapacitor studies. *ACS Appl. Mater. Inter.* **4,** 2242 (2012).
33. Chabot, V. *et al.* A review of graphene and graphene oxide sponge: material synthesis and applications to energy and the environment. *Energy Environ. Sci.* **7,** 1564 (2014).
34. Wang, Y., Zhang, D., Bao, Q., Wu, J. & Wan, Y. Controlled drug release characteristics and enhanced antibacterial effect of graphene oxide–drug intercalated layered double hydroxide hybrid films. *J. Mater. Chem.* **22,** 23106 (2012).
35. Wang, L. *et al.* Layered assembly of graphene oxide and Co–Al layered double hydroxide nanosheets as electrode materials for supercapacitors *Chem. Commun.* **47,** 3556 (2011).
36. Dong, X., Wang, L., Wang, D., Li, C. & Jin, J. Layer-by-layer engineered Co–Al hydroxide nanosheets/graphene multilayer films as flexible electrode for supercapacitor. *Langmuir: the ACS journal of surfaces and colloids* **28,** 293 (2012).
37. Li, M. *et al.* Facile synthesis of NiAl-layered double hydroxide/graphene hybrid with enhanced electrochemical properties for detection of dopamine. *Nanoscale* **3,** 4240 (2011).
38. Wang, Y. *et al.* Enhanced conductivity of a glassy carbon electrode modified with a graphene-doped film of layered double hydroxides for selectively sensing of dopamine. *Microchim. Acta* **174,** 41 (2011).
39. Wu, X.-L., Wang, L., Chen, C.-L., Xu, A.-W. & Wang, X.-K. Water-dispersible magnetite-graphene-LDH composites for efficient arsenate removal. *J. Mater. Chem.* **21,** 17353 (2011).
40. Wang, J. *et al.* Synthesis of layered double hydroxides/graphene oxide nanocomposite as a novel high-temperature CO_2 adsorbent. *J. Energ. Chem.* **24,** 127 (2015).
41. Garcia-Gallastegui, A. *et al.* Graphene Oxide as Support for Layered Double Hydroxides: Enhancing the CO_2 Adsorption Capacity. *Chem. Mater.* **24,** 4531 (2012).
42. Guo, Y. *et al.* Cyclodextrin functionalized graphene nanosheets with high supramolecular recognition capability: synthesis and host−guest inclusion for enhanced electrochemical performance. *ACS Nano.* **4,** 4001 (2010).
43. Liu, S., Tian, J., Wang, L., Luo, Y. & Sun, X. One-pot synthesis of CuO nanoflower-decorated reduced graphene oxide and its application to photocatalytic degradation of dyes. *Catal. Sci. Technol.* **2,** 339 (2012).
44. Hu, Z.-A. *et al.* Synthesis and electrochemical characterization of mesoporous $Co_xNi_{1−x}$ layered double hydroxides as electrode materials for supercapacitors. *Electrochim. Acta* **54,** 2737 (2009).
45. Xu, J. *et al.* A sandwich-type three-dimensional layered double hydroxide nanosheet array/graphene composite: fabrication and high supercapacitor performance. *J. Mater. Chem. A* **2,** 1022 (2014).
46. Park, S. *et al.* Hydrazine-reduction of graphite-and graphene oxide. *Carbon* **49,** 3019 (2011).
47. Palomares, A. E., Uzcátegui, A. & Corma, A. NO_x storage/reduction catalysts based in cobalt/copper hydrotalcites. *Catal. Today* **137,** 261–266, 2007.12.137 (2008).
48. Büchel, R., Strobel, R., Baiker, A. & Pratsinis, S. E. Flame-Made $Pt/K/Al_2O_3$ for NO_x Storage–Reduction (NSR) Catalysts. *Top. Catal.* **52,** 1799 (2009).
49. Zou, Z.-Q., Meng, M. & He, J.-J. Surface distribution state and storage performance of the potassium species in the lean-burn NO_x trap catalyst $Pt/K/Al_2O_3-TiO_2-ZrO_2$. *Mater. Chem. Phys.* **124,** 987 (2010).
50. Castoldi, L. *et al.* Alkaline-and alkaline-earth oxides based Lean NO_x Traps: Effect of the storage component on the catalytic reactivity. *Chem. Eng. J.* **161,** 416 (2010).
51. Prinetto, F., Manzoli, M., Morandi, S., Frola, F. & Ghiotti, G. J. $Pt-K/Al_2O_3$ NSR Catalysts: Characterization of Morphological, Structural and Surface Properties. *Phys. Chem. C* **114,** 1127 (2009).
52. Kim, I. Y. *et al.* A strong electronic coupling between graphene nanosheets and layered titanate nanoplates: a soft-chemical route to highly porous nanocomposites with improved photocatalytic activity. *Small* **8,** 1038 (2012).
53. Lee, Y. R., Kim, I. Y., Kim, T. W., Lee, J. M. & Hwang, S.-J. Mixed colloidal suspensions of reduced graphene oxide and layered metal oxide nanosheets: useful precursors for the porous nanocomposites and hybrid films of graphene/metal oxide. *Chem. Eur. J.* **18,** 2263 (2012).
54. Huang, Z., Wu, P., Gong, B., Fang, Y. & Zhu, N. Fabrication and photocatalytic properties of a visible-light responsive nanohybrid based on self-assembly of carboxyl graphene and ZnAl layered double hydroxides. *J. Mater. Chem.* **2,** 5534 (2014).

55. Li, L. *et al.* Layer-by-layer assembly and spontaneous flocculation of oppositely charged oxide and hydroxide nanosheets into inorganic sandwich layered materials. *J. Am. Chem. Soc.* **129,** 8000 (2007).
56. Gunjakar, J. L., Kim, I. Y., Lee, J. M., Lee, N. S. & Hwang, S. J. Self-assembly of layered double hydroxide 2D nanoplates with graphene nanosheets: an effective way to improve the photocatalytic activity of 2D nanostructured materials for visible light-induced O_2 generation. *Energy Environ. Sci.* **6,** 1008 (2013).
57. Wang, Q. *et al.* Polypropylene/layered double hydroxide nanocomposites. *J. Mater. Chem.* **22,** 19113 (2012).
58. You, R. *et al.* A series of ceria supported lean-burn NO_x trap catalysts $LaCoO_3/K_2CO_3/CeO_2$ using perovskite as active component. *Chem. Eng. J.* **260,** 357 (2015).
59. Fang, J. *et al.* Microwave-assisted synthesis of CoAl-layered double hydroxide/graphene oxide composite and its application in supercapacitors. *Electrochim. Acta* **85,** 248 (2012).
60. Zhou, W. *et al.* One-step synthesis of Ni_3S_2 nanorod@$Ni(OH)_2$ nanosheet core–shell nanostructures on a three-dimensional graphene network for high-performance supercapacitors. *Energy Environ. Sci.* **6,** 2216 (2013).
61. Zhao, X., Cao, J.-P., Zhao, J., Hu, G.-H. & Dang, Z.-M. A hybrid Mg–Al layered double hydroxide/graphene nanostructure obtained via hydrothermal synthesis. *Chem. Phys. Lett.* **605,** 77 (2014).
62. Mei, X., Wang, J., Yang, R., Yan, Q. & Wang, Q. Synthesis of Pt doped Mg-Al layered double oxide/graphene oxide hybrid as novel NO_x storage-reduction catalyst *RSC Adv.* **5,** 78061 (2015).
63. Li, Y., Gao, W., Ci, L., Wang, C. & Ajayan, P. M. Catalytic performance of Pt nanoparticles on reduced graphene oxide for methanol electro-oxidation. *Carbon* **48,** 1124 (2010).
64. Williams, G., Seger, B. & Kamat, P. V. TiO_2-graphene nanocomposites. UV-assisted photocatalytic reduction of graphene oxide. *ACS Nano.* **2,** 1487 (2008).
65. Zhang, Z., Mou, Z., Yu, P., Zhang, Y. & Ni, X. Diesel soot combustion on potassium promoted hydrotalcite-based mixed oxide catalysts. *Catal. Commun.* **8,** 1621 (2007).
66. Ura, B. *et al.* Effect of potassium addition on catalytic activity of $SrTiO_3$ catalyst for diesel soot combustion. *Appl. Catal. B: Environ.* **101,** 169 (2011).
67. Becerra, M. E. *et al.* Soot combustion manganese catalysts prepared by thermal decomposition of $KMnO_4$. *Appl. Catal. B: Environ.* **102,** 260 (2011).
68. Lietti, L., Forzatti, P., Nova, I. & Tronconi, E. NO_x Storage Reduction over Pt/Ba/γ-Al_2O_3 Catalyst *J. Catal.* **204,** 175 (2001).
69. Epling, W. S., Campbell, G. C. & Parks, J. E. The Effects of CO_2 and H_2O on the NO_x Destruction Performance of a Model NO_x Storage/Reduction Catalyst. *Catal. Lett.* **90,** 45 (2003).
70. Huang, H. Y., Long, R. Q. & Yang, R. T. A highly sulfur resistant Pt-Rh/TiO_2/Al_2O_3 storage catalyst for NO_x reduction under lean-rich cycles. *Appl. Catal. B: Environ.* **33,** 127 (2001).
71. Eberhardt, W. *et al.* Photoemission from mass-selected monodispersed Pt clusters. *Phys. Rev. Lett.* **64,** 780 (1990).
72. Bera, P., Patil, K. C., Jayaram, V., Subbanna, G. N. & Hegde, M. S. Ionic dispersion of Pt and Pd on CeO_2 by combustion method: Effect of metal–ceria interaction on catalytic activities for NO reduction and CO and hydrocarbon oxidation. *J. Catal.* **196,** 293 (2000).
73. Arico, A. S. *et al.* An XPS study on oxidation states of Pt and its alloys with Co and Cr and its relevance to electroreduction of oxygen. *Appl. Surf. Sci.* **172,** 33 (2001).
74. Rao, M. M., Reddy, B. R., Jayalakshmi, M., Jaya, V. S. & Sridhar, B. Hydrothermal synthesis of Mg–Al hydrotalcites by urea hydrolysis. *Mater. Res. Bull.* **40,** 347 (2005).
75. Pavel, O. D. *et al.* The activity of Mg/Al reconstructed hydrotalcites by "memory effect" in the cyanoethylation reaction. *Catal. Commun.* **9,** 1974 (2008).
76. Zhao, Y. *et al.* Enhanced antimicrobial properties, cytocompatibility, and corrosion resistance of plasma-modified biodegradable magnesium alloys. *Acta Biomater.* **10,** 544 (2014).
77. Wang, Q. *et al.* High temperature adsorption of CO_2 on Mg–Al hydrotalcite: effect of the charge compensating anions and the synthesis pH. *Catal. Today* **164,** 198 (2011).

Acknowledgements

Author Contributions

X.M. carried out most of the experiments and the analysis of data, and prepared the manuscript. Q.Y. helped with some of the experiments reported; P.L., J.W., Y.C., Y.N. and U.A. assisted with data analysis and discussion, and manuscript preparation. Q.W. designed the experiments, analyzed the data, and prepared the manuscript.

Additional Information

Supplementary information accompanies this paper at http://www.nature.com/srep

Competing financial interests: The authors declare no competing financial interests.

How to cite this article: Mei, X. *et al.* Synthesis of Pt/K_2CO_3/$MgAlO_x$–reduced graphene oxide hybrids as promising NO_x storage–reduction catalysts with superior catalytic performance. *Sci. Rep.* **7,** 42862; doi: 10.1038/srep42862 (2017).

Publisher's note: Springer Nature remains neutral with regard to jurisdictional claims in published maps and institutional affiliations.